

Discovery of a correlation between the frequency of the mHz quasi-periodic oscillations and the neutron-star temperature in the low-mass X-ray binary 4U 1636–53

Ming Lyu^{1*}, Mariano Méndez¹ and Diego Altamirano²

¹*Kapteyn Astronomical Institute, University of Groningen, PO BOX 800, NL-9700 AV Groningen, the Netherlands*

²*School of Physics and Astronomy, University of Southampton, Southampton, SO17 1BJ, UK*

Accepted XXXX. Received XXXX; in original form XXXX

ABSTRACT

We detected millihertz quasi-periodic oscillations (QPOs) in an XMM-Newton observation of the neutron-star low-mass X-ray binary 4U 1636–53. These QPOs have been interpreted as marginally-stable burning on the neutron-star surface. At the beginning of the observation the QPO was at around 8 mHz, together with a possible second harmonic. About 12 ks into the observation a type I X-ray burst occurred and the QPO disappeared; the QPO reappeared ~ 25 ks after the burst and it was present until the end of the observation. We divided the observation into four segments to study the evolution of the spectral properties of the source during intervals with and without mHz QPO. We find that the temperature of the neutron-star surface increases from the QPO segment to the non-QPO segment, and vice versa. We also find a strong correlation between the frequency of the mHz QPO and the temperature of a black-body component in the energy spectrum representing the temperature of neutron-star surface. Our results are consistent with previous results that the frequency of the mHz QPO depends on the variation of the heat flux from the neutron star crust, and therefore supports the suggestion that the observed QPO frequency drifts could be caused by the cooling of deeper layers.

Key words: X-rays: binaries; stars: neutron; accretion, accretion discs; X-rays: individual: 4U 1636–53

1 INTRODUCTION

A class of quasi-periodic oscillations (QPOs) at frequencies of a few mHz were first detected by Revnivtsev et al. (2001) in three neutron-star low-mass X-ray binaries (LMXBs), 4U 1608–52, 4U 1636–53, and Aql X-1. The low frequency range (7 – 9 mHz) spanned by these QPOs, and the strong flux variations at low photon energies (< 5 keV), made them different from other QPOs found in neutron star systems, e.g., the kilohertz (kHz) QPOs (see, e.g., van der Klis 2000; Méndez 2000; Méndez et al. 2001; Belloni et al. 2005; Linares et al. 2005; Jonker et al. 2005; Boutloukos et al. 2006; Méndez 2006; van der Klis 2006; Altamirano et al. 2008; Sanna et al. 2010) and Low-frequency QPOs (see, e.g., Wijnands & van der Klis 1999; Psaltis et al. 1999; Belloni et al. 2002; van Straaten et al. 2002, 2003; van der Klis 2004; Altamirano et al. 2005, 2008, 2012). The mHz QPOs appear only when the source covers a particular range of X-ray luminosities, $L_{2-20\text{keV}} \simeq$

$(5 - 11) \times 10^{36}$ ergs s^{-1} , and the QPOs become undetectable after a type I X-ray burst (Revnivtsev et al. 2001; Altamirano et al. 2008). Those unique observational features suggest that the mechanism responsible for the mHz QPOs is different from the one that produces the other QPOs.

Revnivtsev et al. (2001) proposed that the mHz QPOs were due to a special mode of nuclear burning on the neutron star surface, which only occurs within a certain range of mass accretion rate. Yu & van der Klis (2002) found that in 4U 1608–52 the frequency of the kHz QPO was anticorrelated with the 2 – 5 keV X-ray count rate associated with a 7.5 mHz QPO present in the same observation. This result further supported the nuclear burning interpretation of the mHz QPOs: The inner disc is slightly pushed outward in each mHz QPO cycle by the stresses of radiation coming from the neutron star surface as the luminosity increases.

Heger et al. (2007) proposed that the mHz QPOs are due to marginally stable nuclear burning of Helium on the surface of accreting neutron stars. The characteristic timescale of the oscillations in this model is close to the ge-

* E-mail: m.lyu@astro.rug.nl

ometric mean of the thermal and accretion timescales for the burning layer, $(t_{therm} \times t_{accr})^{1/2}$, about 100 seconds, remarkably consistent with the 2 minutes period of the mHz QPOs. Notwithstanding, the marginally stable burning in the model of Heger et al. (2007) occurs only within a narrow range of mass accretion rate, close to the Eddington rate, one order of magnitude higher than the value implied by the average X-ray luminosity. If the model is correct, the local accretion rate at the burning depth can be higher than the global accretion rate.

Altamirano et al. (2008) found that the frequency of the mHz QPO in 4U 1636–53 systematically decreases with time until the QPO disappears before a type I X-ray burst. This behaviour further supported the idea that the mHz QPOs are closely related to nuclear burning on the neutron star surface. In addition, the work by Altamirano et al. (2008) offered a way to predict the occurrence of X-ray bursts by measuring the frequency of the mHz QPOs. Linares et al. (2010) detected a mHz QPO at a frequency of about 4.5 mHz in the neutron star transient source IGR J17480-2446 in the globular cluster Terzan 5. The persistent luminosity of this source when mHz QPOs were observed was $L_{2-50keV} \sim 10^{38} \text{ erg s}^{-1}$, about an order of magnitude higher than that observed in previous mHz QPO sources. Linares et al. (2012) found that in IGR J17480-2446 the thermonuclear bursts smoothly evolved into a mHz QPO when accretion rate increased, and vice versa. This evolution is predicted by the one-zone models and simulations of the marginally stable burning by Heger et al. (2007), further supporting the idea that the mHz QPO in IGR J17480-2446 is due to marginally stable burning on the neutron star surface.

Keek et al. (2009) showed that turbulent chemical mixing of the accreted fuel combined with a higher heat flux from the crust is able to explain the observed critical accretion rate at which mHz QPOs are observed, and that the frequency drift before X-ray bursts could be due to the cooling of the deep layers where the quasi-stable burning takes place. Furthermore, Keek et al. (2014) investigated how the transition between unstable and stable nuclear burning is influenced by the composition of the accreted material and nuclear reaction rates, and concluded that no allowed variation in accretion composition and reaction rate is able to generate a transition between burning regimes at the observed accretion rate.

4U 1636–53 is a neutron-star LMXB with a 0.1-0.25 M_{\odot} star companion, located at a distance of about 6 kpc (Giles et al. 2002; Galloway et al. 2006). Its orbital period is about 3.8 hr (Pedersen et al. 1982), and the system harbours a neutron star with a spin frequency of 581 Hz (Zhang et al. 1997; Strohmayer 2002). In addition to the mHz QPOs, the source shows all kinds of X-ray bursts (e.g. Galloway et al. 2008; Zhang et al. 2011) and also the full range of spectral states of the persistent emission (Di Salvo et al. 2003; Belloni et al. 2007; Altamirano et al. 2008), making it an excellent candidate to explore the relation between the mHz QPOs and X-ray bursts, and also the spectral properties of the source in the mHz QPO cycle.

Since they are likely related to nuclear burning on the neutron star surface, the spectral and timing analysis of the mHz QPOs provides an insight into their origin and the process of marginally stable nuclear burning on the accreting neutron star surface. In this work, we investigate the

frequency behaviour of the mHz QPO before an X-ray burst, and the reappearance of the QPO after the burst using one XMM observation. Thanks to the low energy coverage of the XMM data, this is the first time that the mHz QPOs have been investigated below $\sim 3 \text{ keV}$, and down to $\sim 0.8 \text{ keV}$. We also study the properties of the source spectrum in different segments with and without mHz QPO before and after the X-ray burst.

2 OBSERVATION AND DATA REDUCTION

We used an XMM-Newton observation of 4U 1636–53 (ObsID 0606070301) performed on September 5, 2009. The data were collected with the European Photon Imaging Camera, EPIC-PN, using the Timing mode, with a total duration of 43.2 ks. The EPIC cameras cover the 0.15-12 keV energy band with a time resolution of 0.03 ms in the timing mode (Strüder et al. 2001).

We reduced the data using the Science Analysis System (SAS) version 13.5.0, with the latest calibration files applied. We fixed some time jumps in the raw event file due to a duplicated packet in the first extension of the EPIC-PN AUX ODF file, following the recommendation of the XMM-Newton EPIC Calibration group. We applied the Rate-Dependent PHA (RDPHA) correction via the command `epproc` to account for the energy scale rate dependence in EPIC-PN Timing mode exposures when producing the calibrated event file. Following the recommendation of the EPIC calibration group, we did not apply the `epfast` correction, since this one was superseded by the RDPHA correction. We used the command `barycen` to convert the arrival time of each photon to the barycenter of the solar system. We found that there was moderate pile up in the observation, and therefore we excluded the central two columns (RAWX=[37,39]) of the PN CCD in the analysis to mitigate these effects. For all light curves and spectra in this work we only selected single and double events (`PATTERN` ≤ 4) for extraction.

2.1 Spectral data

We excluded the events at the edge of the CCD and next to a bad pixel (`FLAG` = 0) to produce the spectra. We generated the redistribution matrix file (RMF) and the ancillary response file (ARF) using `rmfgen` and `arfgen`, respectively, for the latter using the extended point spread function (PSF) model to calculate the encircled energy correction. Since the whole region of the CCD was contaminated by source photons, we extracted the background spectrum from another timing mode observation of the black-hole candidate GX 339–4 (ObsID 0085680601) when the source was in quiescence, on the basis of similar sky coordinates and column density along the line of sight (For more details on the methodology used for the extraction of the background spectrum, please refer to Hiemstra et al. (2011) and Sanna et al. (2013)). Finally, we rebinned the spectra to have at least 25 counts per background-subtracted channel, with an over-sampling of the energy resolution of the PN detector of a factor of 3, and fitted all spectrums in 0.8-11 keV range.

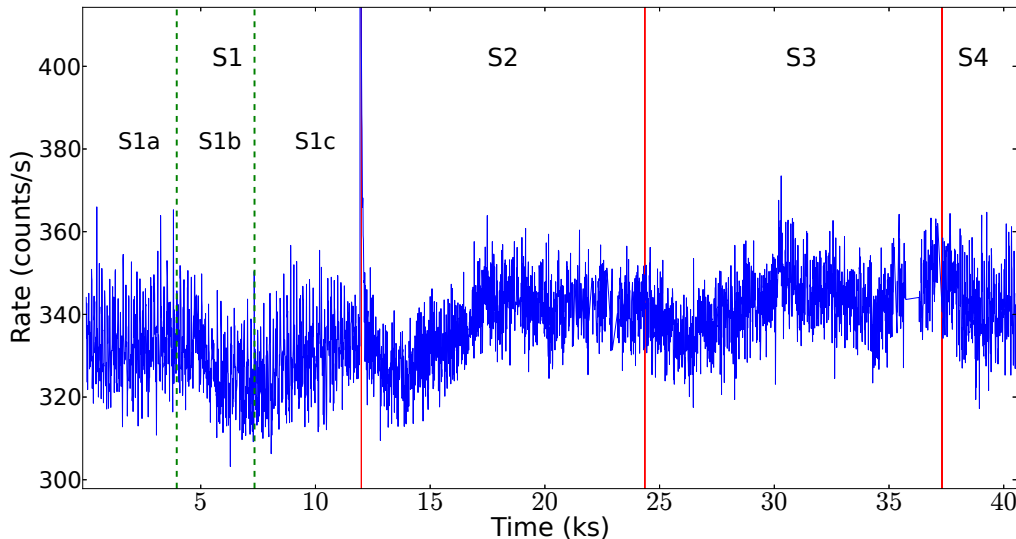


Figure 1. Light curve of 4U 1636–53 with XMM-Newton PN in the 0.8–11 keV range. The time resolution is 10 seconds. Each segment is marked with the name (S1–S4) in the plot; the red vertical lines indicate the borders between the segments. The two green dashed lines show the boundaries between the three subsegments (S1a–S1c) in the first segment. A type I X-ray burst happens at about 12 ks from the start of the observation.

2.2 Timing data

We generated a 1-s resolution light curve (we show a 10-s resolution light curve in Figure 1 for clarity) and an average power spectrum (Figure 2) of the whole observation in the 0.8–11 keV range, after excluding instrument dropouts and an X-ray burst that took place ~ 12 ks from the start of the observation. To produce the average power spectrum of the observation, we calculated the Fourier transform of intervals of 512-s duration using the command `sitar_avg_psd` in the ISIS Version 1.6.2-27 (Houck & Denicola 2000), and rebinned the average power density spectrum logarithmically via the command `sitar_lbin_psd`. The frequency range of the power spectrum is from 1.95×10^{-3} to 0.5 Hz. A strong QPO at about 7–8 mHz and its second harmonic are apparent in the power spectrum (see Figure 2).

To account for the possible evolution of the frequency of this QPO, which we call the mHz QPO, we divided the observation into 71 overlapping time intervals and calculated a dynamic power spectrum oversampling the frequency scale by a factor of 100 using the Lomb-Scargle periodogram method (Lomb 1976; Scargle 1982). Each time interval in the dynamic power spectrum was 1130 seconds long, with the next interval starting 565 s after the start time of the previous interval. We set the count rate of bad time intervals due to the X-ray burst and instrument dropouts in the light curve to the average count rate ($340 \text{ counts s}^{-1}$), the final dynamic power spectrum is shown in Figure 3.

From Figure 3 it is apparent that the mHz QPO is present only at the beginning and at the end of the observation. Guided by this plot, we divided the whole observation into four segments, three of them (S1–S3) of similar length (~ 12 ks), and the last one (S4) covering the remaining ~ 3.5 ks of the observation. The QPO is present in the first and the last segments (S1 and S4), while it is not detected

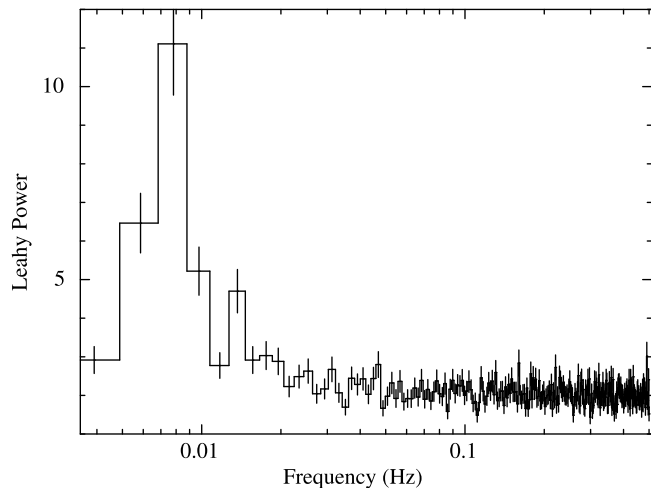


Figure 2. Average power spectrum of the total observation of 4U 1636–53 in the 0.8–11 keV range, calculated from the PN light curve at 1-second resolution. The power spectrum was rebinned logarithmically for clarity. A significant QPO at about 7–8 mHz and its harmonic signal are apparent in the plot.

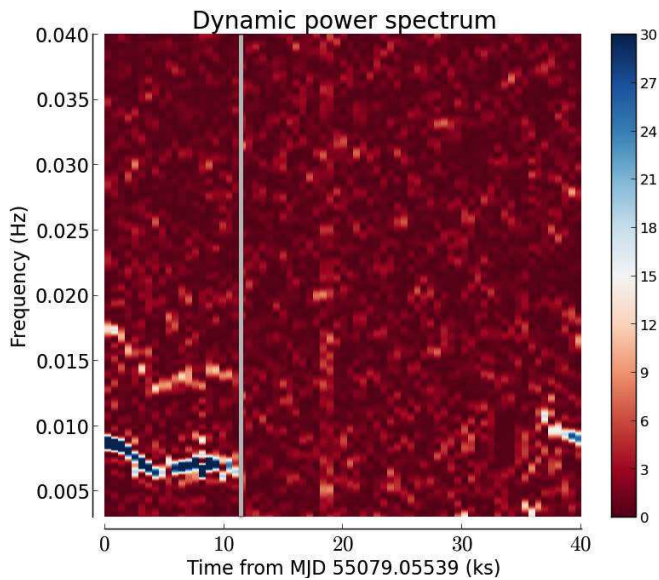
in the second and third ones (S2 and S3; see §3.1). We extracted a light curve and an average power spectrum from each segment; the details of the four segments are listed in Table 1.

We further divided the first segment, before the X-ray burst, into three subsegments, S1a, S1b and S1c, according to the behaviour of the QPO frequency, and generated one light curve for each subsegment. The time intervals of each subsegment were S1a: 0–3954 s, S1b: 3954–7344 s and S1c: 7344–11579 s, respectively, from the start of the observation (MJD=55079.05539).

Table 1. Information for the four segments in which we divided the XMM-Newton observation of 4U 1636–53.

Segment number	Length (ks)	Exposure time (ks) ¹	Average count rate (counts s ⁻¹) ²	mHz QPO
S1	12	11.69	331±20	Yes
S2	12.36	11.38	338±20	No
S3	12.95	11.92	342±19	No
S4	3.49	3.427	342±20	Yes

(1) The final exposure time excludes X-ray bursts, background flares and instrument dropouts. (2) Here we give the standard deviation of the count rate in each segment.

**Figure 3.** Dynamic power spectrum of the XMM-Newton observation of 4U 1636–53. The gray vertical line indicates the time of an X-ray burst in the observation. Each column represents the power spectrum extracted from a time interval of 1130 seconds with the starting time of each segment set to 565 s after the starting time of the previous segment. The frequency scale was over-sampled by a factor of 100 using the Lomb-Scargle periodogram to display the evolution of the mHz QPO frequency. The count rate in bad time intervals due to the X-ray burst and instrument dropouts was fixed to the average count rate of 340 counts s⁻¹. In total, there are 71 power spectra shown in the plot. The colour bar on the right indicates the power at each frequency as defined in the Lomb-Scargle periodogram.

We fitted the total average power spectra using the model `CONSTANT+LORENTZ+LORENTZ`. The `CONSTANT` describes the Poisson noise level, and the first `LORENTZ` component represents the QPO around 7–8 mHz, while the second one represents its second harmonic component. We linked the frequency and width of the second `LORENTZ` component to be the double and the same as in the first `LORENTZ` component, respectively. For segments 2 and 3, where no QPO is detected, we fitted the average power spectra using the model `CONSTANT+LORENTZ` to calculate the upper limit of the rms amplitude of the QPO. We fixed the frequency and the width of the `LORENTZ` component to be the values in the total observation since they are poorly constrained due to the short time ranges (<12 ks). For the three subsegments and the last segment, due to their limited observational time

span (≤ 4.5 ks), we explored the timing properties of the QPO from the light curves: We fitted the light curve of each independent 1130 s time interval in S1 and S4 using a model consisting of a constant plus a sine function. And then we calculated the average frequency and its standard deviation in S1a, S1b, S1c and S4 from the frequencies in the corresponding intervals. Furthermore, we used average frequency to generate a folded light curve for each subsegments and the last segment, and derived the rms amplitude from the fits of the folded light curves.

3 RESULTS

3.1 Timing results

In Figure 1 we plot the light curve of the observation. The length of the light curve is about 40.8 ks, with an average count rate of about 340 counts s⁻¹. In Figure 2 we show the average power spectrum of the total observation. We found a strong QPO at around 7–8 mHz and a possible second harmonic component at ~ 15 mHz. In the dynamic power spectrum we detect the mHz QPO and the second harmonic from the start of the observation until an X-ray burst occurs (around 12 ks in the plot). After the burst, the mHz QPO disappears for about 25.3 ks, and then reappears in the last 3.5 ks of the observation. We estimated the significance of the signal against the hypothesis of white noise via the Lomb-Scargle method. The false alarm probability of the QPO detection (without considering the harmonic) in the total observation is 2.21×10^{-8} , while the probability is 5.24×10^{-19} for segments 1 and 4.

For the total observation, the central frequency of the `LORENTZ` component is $7.2^{+0.4}_{-0.2}$ mHz, with a full-width at half maximum of $2.3^{+1}_{-0.7}$ mHz. The rms amplitude is $1.11 \pm 0.31\%$, which is consistent with the previous measurements (Revnivtsev et al. 2001; Altamirano et al. 2008), although note that Revnivtsev et al. (2001) and Altamirano et al. (2008) used RXTE data which samples > 3 keV range, while we use 0.8–11 keV here. In segments 2 and 3, where no QPO is significantly detected, the 95% upper limit of the rms amplitude is 0.49% and 0.40%, respectively. The average frequency of the mHz QPO decreases from 8.3 mHz in S1a to 6.7 mHz in S1b, and increases slightly to 6.9 mHz in the S1c, before the X-ray burst. After the burst, the QPO reappears at an average frequency of 9.4 mHz in segment 4. The rms amplitude of the QPO increases from $0.80 \pm 0.10\%$ in S1a to $2.27 \pm 0.10\%$ in S1c, and then it is $1.34 \pm 0.10\%$ in segment 4, when it reappears ~ 25 ks after the X-ray burst. The parameters of the mHz QPO are given in Table 2.

Table 2. Parameters of the QPO in the first three subsegments (S1a, S1b and S1c) and the last segment of the observation of 4U 1636–53. Here we give the standard deviation of the average frequency due to its large variation in the subsegments. All errors and upper limits in the Tables are, respectively, at the 90% and 95% confidence level unless otherwise indicated.

	Average frequency (mHz)	RMS amplitude (%)
S1a	8.3 ± 0.6	0.80 ± 0.10
S1b	6.7 ± 0.2	1.48 ± 0.12
S1c	6.9 ± 0.2	2.27 ± 0.10
S4	9.4 ± 0.3	1.34 ± 0.10

3.2 Spectral results

In all our fits, we first tried either a single thermal component (blackbody or disc), or a single Comptonised component to describe the continuum; the results, however, showed that the spectra could not be well fitted with only one of those component. We found that both a thermal and a Comptonised component were necessary to fit the continuum, whereas two thermal components plus a Comptonised component (e.g., Sanna et al. 2013; Lyu et al. 2014) was too complex a model given the quality of the data. For the thermal component either a blackbody or an accretion-disc model could fit the data well. We used either the BBODY component in XSPEC 12.8.1 (Arnaud 1996) to describe the combined thermal emission from the neutron star surface and its boundary layer, or the DISKBB component (Mitsuda et al. 1984; Makishima et al. 1986) to model the multi-temperature thermal emission from an accretion disc. The Comptonised component was modelled by NTHCOMP (Zdziarski et al. 1996; Życki et al. 1999), which describes the emission originating from the inverse Compton scattering process in the corona, with the seed thermal photons coming either from the accretion disc or the neutron star surface (plus boundary layer). In this work we chose the disc as the source of seed photons for the scattering in the corona (Sanna et al. 2013; Lyu et al. 2014). We also included the component PHABS in all our models to account for absorption from the interstellar material along the line of sight. For this component we used the solar abundance table of Wilms et al. (2000) and the photoionization cross section table of Verner et al. (1996). We added a 0.5 % systematic error to the model.

After fitting the spectra with these continuum models in all cases we found significant residuals around 6 – 7 keV, where possible emission from an iron line is expected (Pandel et al. 2008; Cackett et al. 2010; Sanna et al. 2013; Lyu et al. 2014), we therefore added a line component to the model with the central energy of the line constrained to the range 6.4 – 6.97 keV. We first used a Gaussian line to estimate some general properties of the iron line. The fitted width of the line (σ) was between 1.1 keV and 1.6 keV, indicating that a broadening mechanism was required to explain the line profile. We therefore also used the emission line model, KYRLINE (Dovčiak et al. 2004), instead of the Gaussian to fit the iron line. The KYRLINE component describes a relativistic line from an accretion disc around a black hole with arbitrary spin. In this work we fixed the spin parameter at 0.27, which was derived from the spin frequency of the

neutron star (see Sanna et al. (2013) and Lyu et al. (2014) for details), while the outer radius of the disc was fixed at $1000GM/c^2$, where G is the gravitational constant, M is the mass of neutron star and c is the speed of light.

We noticed that the column density, N_H , in PHABS and the power-law index, Γ , the temperature of the disc seed photons, kT_{dbb} , and the electron temperature, kT_e , in NTHCOMP changed systematically between the fits with the two iron line models, (GAUSS or KYRLINE), which in turn changed the normalisation of the spectral components from one model to the other. These differences, however, did not alter the general trends of the parameters as a function of segment number, but just shifted the relations consistently up or down. These variations are likely due to the lack of data above 12 keV, which leads to some degeneracy between parameters (especially the power-law index and electron temperature of the corona). To mitigate this problem we proceeded as follows:

We defined four models, A to D, in Xspec; the continuum components were PHABS, BBODY and NTHCOMP for models A and B, and PHABS, DISKBB and NTHCOMP for models C and D, respectively. For model A and C, we fitted the line with GAUSS, and for B and D with KYRLINE. For models A and B we fitted the spectra of all segments simultaneously linking N_H , Γ , kT_{dbb} and kT_e across segments in each model separately. For models C and D we did the same, except that we did not link kT_{dbb} . For models B and D, for which we used KYRLINE, we further linked the inclination angle of the accretion disc, θ , to be the same in all segments. The other parameters (see Table 4 and Table A1) were left free between models and segments. After we found the best-fitting parameters for the joint fits with models A and B, we deleted model B (model A) and verified that the parameters obtained from the joint fits gave acceptable fits for model A (model B) only. We did the same for models C and D.

To summarise: We used two models, NTHCOMP + BBODY or NTHCOMP + DISKBB, to fit the continuum, and either a GAUSS or KYRLINE component to describe the iron emission line for the spectra of the four segments. Besides, we fitted all spectra with the two line models simultaneously, linking some parameters between the models and the segments.

Here we only describe the main results of the fit with the BBODY component; The results of the fit with the DISKBB component are shown in Appendix.

In Figure 4 we plot the evolution of the temperature of the BBODY component for the four segments. The blackbody temperature, kT_{bb} , first increases from 0.56 ± 0.01 keV to 0.67 ± 0.01 keV from segment 1 to segment 3, and then decreases to 0.64 ± 0.01 keV in the last segment (all errors represent the 90% confidence range). It appears that kT_{bb} increases from the QPO segment to the non-QPO segment (from S1 to S2), and vice versa (from S4 to S3).

In Figure 5 we show the total unabsorbed flux (0.5–130 keV), the unabsorbed flux of the NTHCOMP component and that of the BBODY component as a function of the segment number. The total flux increases from segment 1 to segment 2, and remains more or less constant in the last three segments, while the flux of NTHCOMP increases from the first segment to the second one, and then remains constant or decreases marginally. The flux of the BBODY component de-

Table 3. Fitting results of 4U 1636–53, linked parameters. Values and errors in the Tables are round off to the first or the second decimals.

Model comp	Parameter	Four segments		Three subsegments
		BBODY + NTHCOMP*	DISKBB + NTHCOMP*	BBODY + NTHCOMP
PHABS	$N_H(10^{22})$	$0.38_{-0.02}^{+0.01}$	0.27 ± 0.01	$0.392_{-0.03}^{+0.004}$
KYRLINE	θ (deg)	86.2 ± 0.9	85.9 ± 1.1	$86.5_{-0.2}^{+1.0}$
NTHCOMP	Γ	1.88 ± 0.01	$2.16_{-0.07}^{+0.02}$	1.92 ± 0.01
	kT_e (keV)	3.08 ± 0.08	$5.5_{-1.1}^{+0.6}$	$3.29_{-0.01}^{+0.2}$
	kT_{dbb} (keV)	$0.24_{-0.02}^{+0.07}$	$-^b$	$0.22_{-0.01}^{+0.03}$
	χ^2_ν (χ^2/dof)	1.09 (1463/1347)	1.16 (1568/1348)	1.01 (1017/1002)

* We used two model combinations, NTHCOMP + BBODY and NTHCOMP + DISKBB, to fit the continuum of the four segments.

^b The temperature of the DISKBB component, not linked in the fit, is therefore shown in Table A1.

Table 4. Fitting results of the four segments of 4U 1636–53 using the continuum model BBODY+NTHCOMP, unlinked parameters. We fit the four segments with two iron line models simultaneously (see text for more details); the χ^2_ν (χ^2/dof) of the fit is 1.09 (1463/1347).

Model comp	Parameter	S1	S2	S3	S4
BBODY	kT (keV)	0.56 ± 0.01	0.65 ± 0.01	0.67 ± 0.01	0.64 ± 0.01
	Normalization (10^{-3})	7.2 ± 0.4	6.6 ± 0.3	7.1 ± 0.2	7.8 ± 0.3
	Flux (10^{-10})	6.2 ± 0.3	5.7 ± 0.2	6.1 ± 0.2	6.7 ± 0.3
NTHCOMP	Normalization	0.87 ± 0.03	0.91 ± 0.03	0.91 ± 0.02	0.90 ± 0.05
	Flux (10^{-10})	57.8 ± 2.8	60.5 ± 2.8	60.9 ± 2.4	59.8 ± 3.6
KYRLINE	R_{in} (R_G)	11.5 ± 2.3	$5.12_{-0}^{+0.27}$	$5.12_{-0}^{+0.12}$	$5.12_{-0}^{+0.41}$
	E_{line} (keV)	$6.97_{-0.15}^{+0}$	6.59 ± 0.14	6.60 ± 0.09	6.85 ± 0.12
	α	3.2 ± 0.5	2.8 ± 0.2	2.8 ± 0.2	2.6 ± 0.2
	Normalization (10^{-3})	4.7 ± 0.6	9.3 ± 0.7	11.5 ± 0.8	9.9 ± 1.2
	Flux (10^{-10})	0.53 ± 0.07	1.02 ± 0.09	1.26 ± 0.09	1.1 ± 0.1
	Total flux (10^{-10})	64.6 ± 2.8	67.2 ± 2.8	68.3 ± 2.4	67.7 ± 3.6
BBODY	kT (keV)	0.56 ± 0.01	0.64 ± 0.01	0.67 ± 0.01	0.64 ± 0.01
	Normalization (10^{-3})	7.3 ± 0.4	6.9 ± 0.3	7.4 ± 0.3	8.0 ± 0.4
	Flux (10^{-10})	6.3 ± 0.3	5.9 ± 0.3	6.4 ± 0.3	6.9 ± 0.3
NTHCOMP	Normalization	0.87 ± 0.03	0.90 ± 0.03	0.91 ± 0.03	0.89 ± 0.05
	Flux (10^{-10})	57.7 ± 2.6	60.0 ± 2.7	60.3 ± 2.7	59.4 ± 3.8
GAUSS	E_{line} (keV)	$6.97_{-0.08}^{+0}$	6.78 ± 0.17	6.84 ± 0.13	$6.97_{-0.12}^{+0}$
	σ (keV)	1.1 ± 0.1	1.6 ± 0.2	1.5 ± 0.1	1.5 ± 0.2
	Normalization (10^{-3})	5.1 ± 0.8	11.3 ± 1.9	13.7 ± 1.8	11.8 ± 1.9
	Flux (10^{-10})	0.57 ± 0.08	1.2 ± 0.2	1.5 ± 0.2	1.3 ± 0.2
	Total flux (10^{-10})	64.6 ± 2.6	67.2 ± 2.7	68.2 ± 2.7	67.6 ± 3.9

creases from segment 1 to segment 2, and then increases in the last three segments.

The best fitting parameters to the spectra of the four segments using BBODY to fit the soft component are shown in Table 3 (linked parameters: N_H , Γ , kT_e , θ and kT_{dbb}) and Table 4 (unlinked parameters), respectively. All errors and upper limits in the Tables are, respectively, at the 90% and 95% confidence level, unless otherwise indicated.

As mentioned in §2.2, we divided the first segment into three subsegments, and we analysed the spectra of S1a, S1b and S1c in the same way as we did for the four segments, except that here we only used the NTHCOMP + BBODY model to describe the continuum, since the mHz QPOs are regarded to be connected to marginal stable burning on the neutron star surface (see §1). The best fitting parameters to the spectra of the three subsegments are given in Table 3 (linked parameters: N_H , Γ , kT_e , θ and kT_{dbb}) and Table 5 (unlinked parameters), respectively.

In Figure 6 we plot the blackbody temperature, kT_{bb} , vs. subsegment number. The blackbody temperature is 0.60 ± 0.01 keV for the GAUSS (0.60 ± 0.02 keV for the KYRLINE) in the S1a, it decreases to 0.58 ± 0.01 keV (0.57 ± 0.02 keV for the KYRLINE) in S1b, and finally it changes to 0.59 ± 0.01 keV (0.59 ± 0.02 keV for the KYRLINE) in the S1c.

In Figure 7 we show the relation between the average frequency of the mHz QPO and the temperature of the blackbody component in the three subsegments and the last segment, where the QPO reappears after the burst. Considering the variation of the frequency in the first subsegment, we plot the standard deviation of the average frequency as error bars in the plot. This Figure shows a clear correlation between the average frequency of the QPO and the temperature of the blackbody component, the correlation coefficient between the frequency and the temperature is 0.95.

Table 5. Fitting results of the first three subsegments of 4U 1636–53 using the continuum model BBODY+NTHCOMP, unlinked parameters. We fit the three subsegments with two iron line models simultaneously (see text for more details); the χ^2_ν (χ^2/dof) of the fit is 1.01 (1017/1002).

Model comp	Parameter	S1a	S1b	S1c
BBODY	kT (keV)	0.60 ± 0.02	0.57 ± 0.02	0.59 ± 0.02
	Normalization (10^{-3})	7.7 ± 0.4	7.2 ± 0.2	$7.18^{+0.5}_{-0.06}$
	Flux (10^{-10})	6.7 ± 0.3	6.2 ± 0.2	6.2 ± 0.2
NTHCOMP	Normalization	0.91 ± 0.04	0.90 ± 0.03	$0.91^{+0.01}_{-0.06}$
	Flux (10^{-10})	58.3 ± 2.4	58.1 ± 2.5	58.4 ± 2.4
KYRLINE	R_{in} (R_G)	$5.12^{+1.28}_{-0}$	$5.12^{+0.52}_{-0}$	$10.0^{+0.3}_{-1.6}$
	E_{line} (keV)	6.46 ± 0.08	6.5 ± 0.1	$6.97^{+0}_{-0.24}$
	α	2.9 ± 0.2	2.5 ± 0.2	3.9 ± 0.3
	Normalization (10^{-3})	$10.23^{+0.8}_{-0.02}$	$7.3^{+1.2}_{-0.3}$	7.5 ± 1.0
	Flux (10^{-10})	1.09 ± 0.05	0.78 ± 0.08	0.8 ± 0.1
	Total flux (10^{-10})	66.1 ± 2.4	65.0 ± 2.5	65.4 ± 2.4
BBODY	kT (keV)	0.60 ± 0.01	0.58 ± 0.01	0.59 ± 0.01
	Normalization (10^{-3})	7.8 ± 0.5	7.2 ± 0.3	7.4 ± 0.2
	Flux (10^{-10})	6.7 ± 0.4	6.2 ± 0.2	6.4 ± 0.2
NTHCOMP	Normalization	$0.90^{+0.01}_{-0.06}$	$0.90^{+0.01}_{-0.06}$	0.90 ± 0.03
	Flux (10^{-10})	58.2 ± 2.5	58.1 ± 2.5	58.0 ± 2.3
GAUSS	E_{line} (keV)	$6.77^{+0.07}_{-0.04}$	$6.79^{+0.07}_{-0.1}$	$6.88^{+0.09}_{-0.2}$
	σ (keV)	$1.37^{+0.1}_{-0.03}$	$1.19^{+0.07}_{-0.2}$	$1.34^{+0.09}_{-0.01}$
	Normalization (10^{-3})	$10.5^{+1.4}_{-0.6}$	$7.1^{+1.5}_{-0.1}$	$8.94^{+1.5}_{-0.3}$
	Flux (10^{-10})	1.2 ± 0.1	0.78 ± 0.09	1.0 ± 0.1
	Total flux (10^{-10})	66.1 ± 2.6	65.1 ± 2.5	65.4 ± 2.3

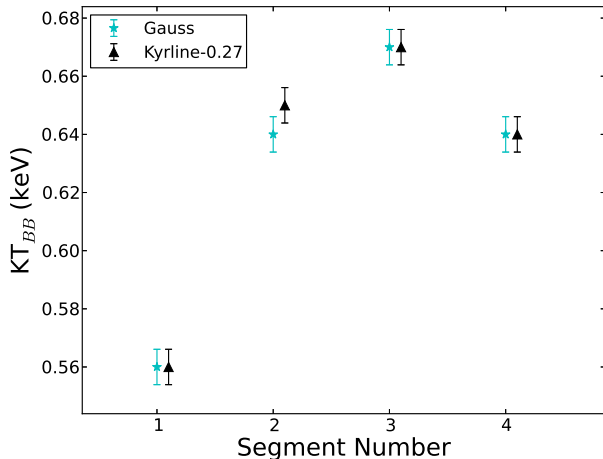


Figure 4. Temperature of the blackbody component in 4U 1636–53 as a function of segment number for the XMM-Newton observation. The model BBODY+NTHCOMP was used to fit the continuum. Different colours/symbols show the results of fits with different models to the iron line, as indicated in the legend, with Kyrline-0.27 representing the results when we fitted the line with a KYRLINE model with the spin parameter fixed to 0.27. In this and other plots an offset in the x -axis between the results of the two iron line models has been added for clarity. Error bars in this and the other plots correspond to the $1\text{-}\sigma$ confidence range.

4 DISCUSSION

We report the first detection of a mHz quasi-periodic oscillation (QPO), in the neutron-star LMXB 4U 1636–53, with

XMM-Newton. At the beginning of the observation the frequency of the mHz QPO was ~ 8.3 mHz, and then the frequency slowly decreased to below ~ 7 mHz. At the time of ~ 12 ks a PRE X-ray burst occurs (Zhang et al. 2011), the mHz QPO disappears, and it subsequently reappears about 25.3 ks later at a frequency of ~ 9.4 mHz. This is the longest time interval so far measured between the disappearance and reappearance of mHz QPO in any LMXB. The 0.8 – 11 keV rms amplitude of the QPO increases from $0.80 \pm 0.06\%$ in S1a to $2.27 \pm 0.06\%$ in S1c just before the X-ray burst, and changes to $1.34 \pm 0.06\%$ when the QPO reappears after the burst. Finally, we discovered a strong correlation between the frequency of the mHz QPO and the temperature of the neutron-star surface, represented by a blackbody component in the energy spectrum of the source.

Using RXTE observations, Altamirano et al. (2008) found that the mHz QPOs in 4U 1636–53 occur only when the source is in certain spectral states: When the source is in an intermediate spectral state, close to the transition between the soft and the hard state (see Figure 1 in Altamirano et al. 2008), 4U 1636–53 exhibits mHz QPOs with frequencies that systematically decrease with time from ~ 15 mHz to around 7 – 9 mHz, and at that frequency the QPOs disappear simultaneously with the occurrence of a Type I X-ray burst. When 4U 1636–53 is in a softer state, the oscillations show no frequency drift, and the frequency is always constrained between ~ 7 and ~ 9 mHz.

The QPO we found in the XMM-Newton observation of 4U 1636–53 shows a frequency drift, from ~ 8.3 mHz to ~ 7 mHz, and disappears after the Type-I X-ray burst onset. As previously reported by Sanna et al. (2013) and Lyu et al. (2014), the XMM-Newton observation analysed in this paper (Obs.5 in Sanna et al. 2013) sampled the transition between

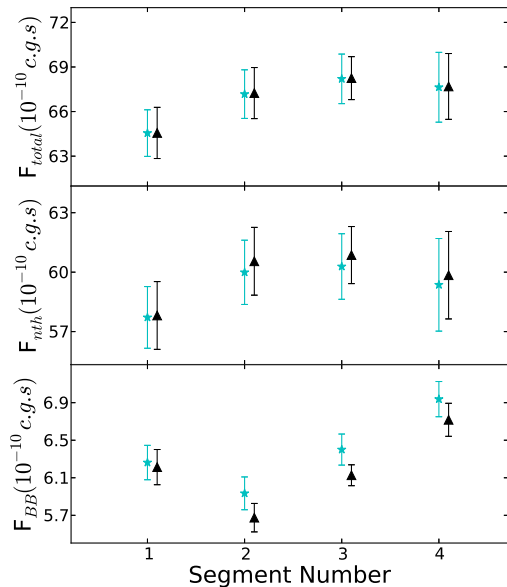


Figure 5. The total unabsorbed flux (top panel), the flux of the NTHCOMP component (middle panel) and the BBODY component (bottom panel) in the 0.5 – 130 keV range for 4U 1636–53 as a function of segment number. The model BBODY+NTHCOMP was used to fit the continuum. Symbols are the same as in Figure 4.

the soft state and the hard state of 4U 1636–53 (see Figure 2 in Sanna et al. 2013). Our results are therefore consistent with the picture that frequency drifts of the mHz QPOs are only observed in the state transition.

Altamirano et al. (2008) also showed that the time interval required to detect the mHz QPOs after an X-ray burst is not always the same, and it is independent of the spectral state of the source. However, due to gaps in the RXTE observations, they could not exclude waiting times as short as ~ 1000 s. Molkov et al. (2005) observed a ~ 10 mHz oscillations in the LMXB SLX 1735–269 that reappeared during the decaying phase of an X-ray burst, just ~ 400 s after the peak of the burst. At the other extreme, Altamirano et al. (2008) found that no mHz QPOs were detected during the ≈ 15 ks of uninterrupted data after an X-ray burst in 4U 1636–53, setting a lower limit on the longest waiting time for this source. In this paper, and thanks to the ability of XMM-Newton to carrying out long observations without data-gaps, we find a waiting time of ~ 25 ks between an X-ray burst and the reappearance of the mHz QPO, the longest waiting time so far.

Standard theory predicts that the transition from stable to unstable helium burning via the triple-alpha process takes place when the accretion rate is close to the Eddington limit (Fujimoto et al. 1981; Ayasli & Joss 1982). If the accreted matter is hydrogen-deficient, the transition is expected to take place at an even higher accretion rate (Bildsten & Cumming 1998; Keek et al. 2009). 4U 1636–53 accretes at few percent of Eddington; however if local mass accretion rate per unit area is $\dot{m} \simeq \dot{m}_{Edd}$, as suggested by Heger et al. (2007), only ≈ 1000 seconds are required to accrete a fuel layer of column

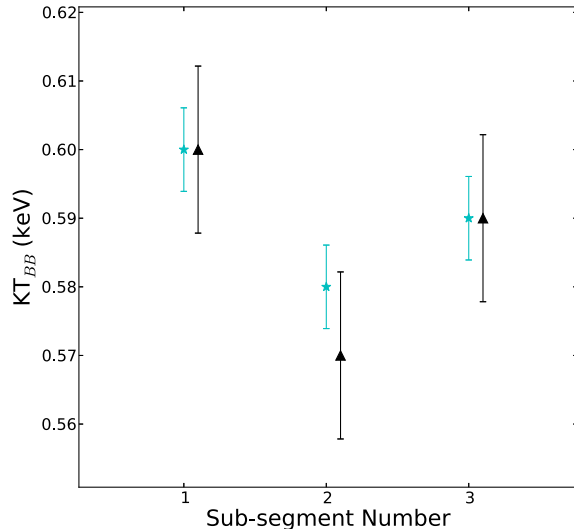


Figure 6. Temperature of the blackbody component in 4U 1636–53 for the first three subsegments (S1a, S1b and S1c) of the XMM-Newton observation. The model BBODY+NTHCOMP was used to fit the continuum. Symbols are the same as in Figure 4.

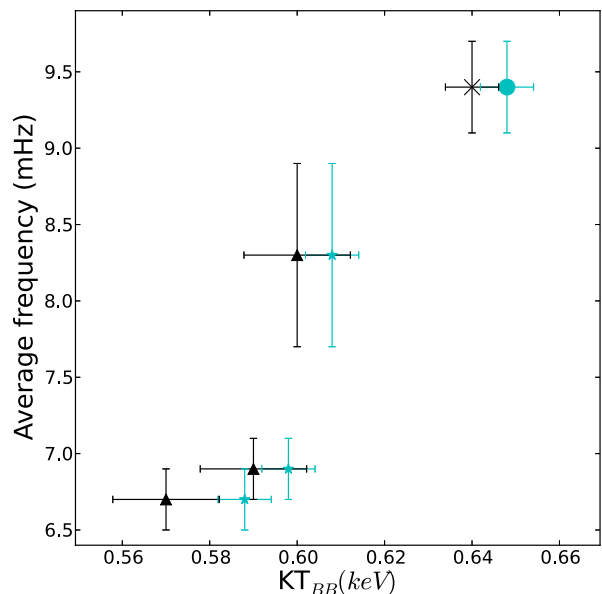


Figure 7. Average frequency of the mHz QPO vs. the temperature of the blackbody component for the first three subsegments and the last segment of the observation of 4U 1636–53. The model BBODY+NTHCOMP was used to fit the continuum. Here we plot the standard deviation of the average frequency. We added an offset of 0.008 keV to the temperature of the blackbody component in the case of GAUSS model for clarity. Symbols are the same as in Figure 4. We use an “X” symbol in black and a filled circle in cyan to show the results of the KYRLINE and the GAUSS iron line model for the segment 4, respectively.

depth y_f capable of undergoing marginally stable burning (assuming that none of the accreting fuel is burnt, $y_f \approx 10^8 \text{ g cm}^{-2}$, and $\dot{m} \approx 8 \times 10^4 \text{ g cm}^{-2} \text{ s}^{-1}$; see, e.g. Heger et al. 2007). Waiting times longer than 1000 s, and particularly as long as ~ 25 ks, imply that at the observed luminosities either a large fraction of the accreted fuel must be burnt as it accretes onto the neutron-star surface (e.g., van Paradijs et al. 1988; Cornelisse et al. 2003; Galloway et al. 2008; Altamirano et al. 2008; Keek et al. 2009, and references therein), or that only a small fraction of the accreted matter reaches the neutron-star surface.

If hydrogen and/or helium can mix efficiently as mass is accreted onto the neutron star, the conditions under which the fuel is burnt are different (e.g., Fujimoto 1993; Yoon et al. 2004; Piro & Bildsten 2007; Keek et al. 2009). Keek et al. (2009) studied the effect of rotationally induced transport processes on the stability of helium burning. They found that as helium is diffused to greater depths, the stability of the burning is increased, such that the critical accretion rate for stable helium burning decreases and, combined with a higher heat flux from the crust, turbulent mixing could explain the fact that mHz QPOs occur at (apparent) lower accretion rates. Furthermore, Keek et al. (2009) found that by lowering the heat flux from the crust (effectively cooling the burning layer), the frequency of the marginally-stable burning decreases. 4U 1636–53 shows mHz QPOs with systematically decreasing frequencies right before a type I X-ray burst (Altamirano et al. 2008). That behaviour of the frequency is considered to be related to the heating of the deeper layers of the neutron star. Here we find a strong correlation between the average frequency of the mHz QPO and the temperature of the blackbody component in the energy spectrum. It is worth mentioning that the blackbody temperature from the fits corresponds to the effective temperature of the neutron-star photosphere rather than the temperature of the burning layer on the neutron star surface. Besides, the blackbody temperature could in fact be partly the temperature of the disc, since we do not fit a disc component and a blackbody component separately, but just a blackbody component that accounts for both components. If the temperature of the burning layer and that of the photosphere are correlated, and the temperature of the disc remains more or less constant during our observation, the frequency of the mHz QPO should be correlated with the temperature of the burning layer. This is different from the prediction of the model of Heger et al. (2007), in which the frequency is inversely proportional to the square root of the temperature of the burning layer. Assuming that mass accretion rate is proportional to the total flux in each segment (see Fig 5), and the thickness of the fuel layer is more or less constant, we found no significant correlation between the observed frequency and the frequency predicted by eq. (11) in Heger et al. (2007). In our data the predicted frequency changes by $\sim 0.5\%$, but the errors are about 5%, which precludes us from drawing any conclusion. On the other hand, a correlation between QPO frequency and neutron-star temperature is consistent with the results of Keek et al. (2009): When the burning layer is effectively cooled down, the frequency of the oscillations decreases by tens of percents until a flash occurs. Interestingly, we find that the frequency-temperature correlation holds also when the mHz QPO reappears after the burst. Additionally, the

model of Keek et al. (2009) could also explain why the mHz QPOs are not sensitive to short-term variations in the accretion rate: The cooling could, for instance, be dominated by the slow release of energy from a deeper layer that was heated up during an X-ray burst (Keek et al. 2009).

Furthermore, Keek et al. (2009) found that the flux from the neutron-star crust, $L_{critical}$, at the transition between stable and unstable burning increases with increasing accretion rate. This may offer a clue about the mechanism that triggers the reappearance of the mHz QPO after the burst. As shown in Figure 5, the total flux in segments 2 to 4, after the X-ray burst, is higher than the total flux in the first segment, before the burst, indicating that the accretion rate may have increased after the burst. If $L_{critical}$ in segment 1 is $L_{critical}^{lo}$, the increase of accretion rate after the X-ray burst would lead to a higher value, $L_{critical}^{hi}$, which in turn sets a higher threshold that needs to be overcome for the mHz QPO to reappear. The flux of the blackbody component (lower panel in Figure 5) in segment 1 is around $6.2 \times 10^{-10} \text{ ergs cm}^{-2} \text{ s}^{-1}$; after the burst the flux drops in segment 2, and after that it increases until the end of the observation. Only segment 4 shows a blackbody flux that is significantly larger than the one in segment 1, indicating that the heat flux from the crust in segment 4 may be as high as the value of $L_{critical}^{hi}$ required for the mHz QPO to reappear. This scenario is also consistent with the prediction of the standard theory: After an X-ray burst fuel on the neutron-star surface becomes hydrogen-deficient, leading to a transition at a higher accretion rate.

ACKNOWLEDGMENTS

This research has made use of data obtained from the High Energy Astrophysics Science Archive Research Center (HEASARC), provided by NASA’s Goddard Space Flight Center. This research made use of NASA’s Astrophysics Data System. LM is supported by China Scholarship Council (CSC), grant number 201208440011. DA acknowledges support from the Royal Society.

APPENDIX A: RESULTS OF THE FIT TO THE FOUR SEGMENTS WITH A DISC COMPONENT

As shown in Table A1 the temperature of the disc is above 0.65 keV in the first and the last segments, where the mHz QPO is detected, while it is below 0.64 keV for the other two segments. The inner radius of the disc pegs at the lower boundary, $5.12R_g$, for all segments, while the emissivity index of the line marginally decreases from about 2.7 in the first three segments to about 2.5 in the fourth one. The width of the GAUSS component appears to decrease slightly in the first three segments, and then increases to 1.5 ± 0.2 in the last segment. The two line models show different results of the energy of the line: The line is at about 6.9 keV in the first segment and then pegs at 6.97 keV in the other segments for the GAUSS model, while in the KYRLINE case the line is between 6.6 keV and 6.7 keV in the first three segments, and then increases to ~ 6.9 keV in the last segment.

Table A1. Fitting results of four segments of 4U 1636–53 using the continuum model DISKBB+NTHCOMP; unlinked parameters. We fit the four segments with two iron line models simultaneously (see text for more details); the χ^2_ν (χ^2/dof) of the fit is 1.16 (1568/1348).

Model comp	Parameter	S1	S2	S3	S4
DISKBB	kT (keV)	0.66 ± 0.02	0.60 ± 0.03	0.61 ± 0.03	0.67 ± 0.02
	Normalization	$151.8^{+29.1}_{-5.6}$	< 48.8	< 47.2	$90.4^{+38.2}_{-17.7}$
	Flux (10^{-10})	5.1 ± 1.8	< 1.07	< 1.14	3.2 ± 2.2
NTHCOMP	Normalization	0.67 ± 0.05	0.83 ± 0.01	$0.83^{+0.01}_{-0.06}$	0.73 ± 0.06
	Flux (10^{-10})	57.6 ± 4.8	66.5 ± 6.2	67.6 ± 4.9	63.5 ± 6.1
KYRLINE	R_{in} (R_G)	$5.12^{+0.18}_{-0}$	$5.12^{+0.21}_{-0}$	$5.12^{+0.20}_{-0}$	$5.12^{+0.43}_{-0}$
	E_{line} (keV)	6.65 ± 0.07	6.69 ± 0.11	6.62 ± 0.09	$6.88^{+0.09}_{-0.1}$
	α	2.7 ± 0.1	2.7 ± 0.2	2.7 ± 0.2	2.5 ± 0.2
	Normalization (10^{-3})	11.4 ± 0.8	10.5 ± 0.8	11.3 ± 0.8	10.6 ± 1.3
	Flux (10^{-10})	1.26 ± 0.08	1.17 ± 0.09	1.24 ± 0.09	1.2 ± 0.1
	Total flux (10^{-10})	63.9 ± 5.1	67.7 ± 6.6	68.9 ± 5.6	68.0 ± 6.4
DISKBB	kT (keV)	0.68 ± 0.02	0.61 ± 0.03	0.61 ± 0.03	0.69 ± 0.03
	Normalization	$164.2^{+24.7}_{-11.0}$	< 66.3	< 40.8	$106.6^{+33.0}_{-17.0}$
	Flux (10^{-10})	6.2 ± 1.9	< 1.53	< 1.00	4.2 ± 2.8
NTHCOMP	Normalization	0.64 ± 0.03	$0.82^{+0.02}_{-0.1}$	$0.83^{+0.01}_{-0.1}$	0.70 ± 0.06
	Flux (10^{-10})	55.9 ± 4.1	66.1 ± 6.5	67.7 ± 7.1	62.0 ± 6.2
GAUSS	E_{line} (keV)	$6.88^{+0.09}_{-0.12}$	$6.97^{+0}_{-0.10}$	$6.97^{+0}_{-0.05}$	$6.97^{+0}_{-0.06}$
	σ (keV)	1.5 ± 0.1	1.4 ± 0.1	1.33 ± 0.08	1.5 ± 0.2
	Normalization (10^{-3})	14.3 ± 2.1	11.0 ± 1.2	11.1 ± 1.0	13.0 ± 2.5
	Flux (10^{-10})	1.6 ± 0.2	1.2 ± 0.1	1.3 ± 0.1	1.5 ± 0.3
	Total flux (10^{-10})	63.7 ± 4.6	67.6 ± 7.1	69.0 ± 7.6	67.7 ± 6.8

The total unabsorbed flux and the flux of the NTHCOMP evolve in a similar way as in the case where we used BBODY+NTHCOMP to fit the continuum: Both fluxes first increase and then remain more or less constant or just decrease slightly in the last segment. The DISKBB component is formally not required in the fits of segments 2 and 3, where there are no mHz QPO present in the data. For the flux of the iron line, in the case of GAUSS, it is slightly lower in segments 2 and 3 where there is no mHz QPO, while in the KYRLINE case the flux of the line is more or less constant in all segments.

The best fitting parameters to the spectra of the four segments using DISKBB to fit the soft component are given in Table 3 (linked parameters: N_H , Γ , kT_e and θ) and Table A1 (unlinked parameters), respectively.

REFERENCES

- Altamirano D., Ingram A., van der Klis M., Wijnands R., Linares M., Homan J., 2012, *ApJ*, 759, L20
- Altamirano D., van der Klis M., Méndez M., Jonker P. G., Klein-Wolt M., Lewin W. H. G., 2008, *ApJ*, 685, 436
- Altamirano D., van der Klis M., Méndez M., Migliari S., Jonker P. G., Tiengo A., Zhang W., 2005, *ApJ*, 633, 358
- Altamirano D., van der Klis M., Méndez M., Wijnands R., Markwardt C., Swank J., 2008, *ApJ*, 687, 488
- Altamirano D., van der Klis M., Wijnands R., Cumming A., 2008, *ApJ*, 673, L35
- Arnaud K. A., 1996, in Jacoby G. H., Barnes J., eds, *Astronomical Data Analysis Software and Systems V* Vol. 101 of *Astronomical Society of the Pacific Conference Series*, XSPEC: The First Ten Years. p. 17
- Ayasli S., Joss P. C., 1982, *ApJ*, 256, 637
- Belloni T., Homan J., Motta S., Ratti E., Méndez M., 2007, *MNRAS*, 379, 247
- Belloni T., Méndez M., Homan J., 2005, *A&A*, 437, 209
- Belloni T., Psaltis D., van der Klis M., 2002, *ApJ*, 572, 392
- Bildsten L., Cumming A., 1998, *ApJ*, 506, 842
- Boutloukos S., van der Klis M., Altamirano D., Klein-Wolt M., Wijnands R., Jonker P. G., Fender R. P., 2006, *ApJ*, 653, 1435
- Cackett E. M., Miller J. M., Ballantyne D. R., Barret D., Bhattacharyya S., Boutelier M., Miller M. C., Strohmayer T. E., Wijnands R., 2010, *ApJ*, 720, 205
- Cornelisse R., in't Zand J. J. M., Verbunt F., Kuulkers E., Heise J., den Hartog P. R., Cocchi M., Natalucci L., Bazzano A., Ubertini P., 2003, *A&A*, 405, 1033
- Di Salvo T., Méndez M., van der Klis M., 2003, *A&A*, 406, 177
- Dovčiak M., Karas V., Yaqoob T., 2004, *ApJS*, 153, 205
- Fujimoto M. Y., 1993, *ApJ*, 419, 768
- Fujimoto M. Y., Hanawa T., Miyaji S., 1981, *ApJ*, 247, 267
- Galloway D. K., Munro M. P., Hartman J. M., Psaltis D., Chakrabarty D., 2008, *ApJS*, 179, 360
- Galloway D. K., Psaltis D., Munro M. P., Chakrabarty D., 2006, *ApJ*, 639, 1033
- Giles A. B., Hill K. M., Strohmayer T. E., Cummings N., 2002, *ApJ*, 568, 279
- Heger A., Cumming A., Woosley S. E., 2007, *ApJ*, 665, 1311
- Hiemstra B., Méndez M., Done C., Díaz Trigo M., Altamirano D., Casella P., 2011, *MNRAS*, 411, 137
- Houck J. C., Denicola L. A., 2000, in Manset N., Veillet C., Crabtree D., eds, *Astronomical Data Analysis Software and Systems IX* Vol. 216 of *Astronomical Society of the Pacific Conference Series*, ISIS: An Interactive Spectral Interpretation System for High Resolution X-Ray Spectroscopy. p. 591
- Jonker P. G., Méndez M., van der Klis M., 2005, *MNRAS*, 360, 921
- Keek L., Cyburt R. H., Heger A., 2014, *ApJ*, 787, 101
- Keek L., Langer N., in't Zand J. J. M., 2009, *A&A*, 502, 871
- Linares M., Altamirano D., Chakrabarty D., Cumming A., Keek L., 2012, *ApJ*, 748, 82
- Linares M., Altamirano D., Watts A., van der Klis M., Wijnands R., Homan J., Casella P., Patruno A., Armas-Padilla M., Cavecchi Y., Degenaar N., Kalamkar M., Kaur R., Yang Y., Rea N., 2010, *The Astronomer's Telegram*, 2958, 1
- Linares M., van der Klis M., Altamirano D., Markwardt C. B., 2005, *ApJ*, 634, 1250
- Lomb N. R., 1976, *Ap&SS*, 39, 447
- Lyu M., Méndez M., Sanna A., Homan J., Belloni T., Hiemstra B., 2014, *MNRAS*, 440, 1165
- Makishima K., Maejima Y., Mitsuda K., Bradt H. V., Remillard R. A., Tuohy I. R., Hoshi R., Nakagawa M., 1986, *ApJ*, 308, 635
- Méndez M., 2000, *Proc 19th Texas Symposium on Relativistic Astrophysics and Cosmology*, ed. J. Paul, T. Montmerle, & E. Aubourg (Amsterdam: Elsevier), 15/16
- Méndez M., 2006, *MNRAS*, 371, 1925
- Méndez M., van der Klis M., Ford E. C., 2001, *ApJ*, 561, 1016
- Mitsuda K., Inoue H., Koyama K., Makishima K., Matsuoka M., Ogawara Y., Suzuki K., Tanaka Y., Shibazaki N., Hirano T., 1984, *PASJ*, 36, 741
- Molkov S., Revnivtsev M., Lutovinov A., Sunyaev R., 2005, *A&A*, 434, 1069
- Pandel D., Kaaret P., Corbel S., 2008, *ApJ*, 688, 1288
- Pedersen H., Lub J., Inoue H., Koyama K., Makishima K., Matsuoka M., Mitsuda K., Murakami T., Oda M., Ogawara Y., Ohashi T., Shibazaki N., Tanaka Y., Hayakawa S., Kunieda H., Makino F., Doty J., Lewin W. H. G., 1982, *ApJ*, 263, 325
- Piro A. L., Bildsten L., 2007, *ApJ*, 663, 1252
- Psaltis D., Belloni T., van der Klis M., 1999, *ApJ*, 520, 262
- Revnivtsev M., Churazov E., Gilfanov M., Sunyaev R., 2001, *A&A*, 372, 138
- Sanna A., Hiemstra B., Méndez M., Altamirano D., Belloni T., Linares M., 2013, *MNRAS*, 432, 1144
- Sanna A., Méndez M., Altamirano D., Homan J., Casella P., Belloni T., Lin D., van der Klis M., Wijnands R., 2010, *MNRAS*, 408, 622
- Scargle J. D., 1982, *ApJ*, 263, 835
- Strohmayer T., 2002, in *APS Meeting Abstracts Discovery of the Millisecond Pulsar in 4U 1636-53 During a Superburst*. p. 17094
- Strüder L., Briel U., Dennerl K., Hartmann R., Kendziorra E., Meidinger N., Pfeiffermann E., Reppin C., Aschenbach B., Bornemann W., Bräuninger H., Burkert W., Elender M., Freyberg M., Haberl F., 2001, *A&A*, 365, L18
- van der Klis M., 2000, *ARA&A*, 38, 717
- van der Klis M., 2004, *ArXiv: astro-ph/0410551*
- van der Klis M., 2006, in *Compact Stellar X-Ray Sources*, ed. W. H. G. Lewin & M. van der Klis (Cambridge: Cambridge Univ. Press)
- van Paradijs J., Penninx W., Lewin W. H. G., 1988, *MNRAS*, 233, 437
- van Straaten S., van der Klis M., di Salvo T., Belloni T., 2002, *ApJ*, 568, 912
- van Straaten S., van der Klis M., Méndez M., 2003, *ApJ*, 596, 1155
- Verner D. A., Ferland G. J., Korista K. T., Yakovlev D. G., 1996, *ApJ*, 465, 487
- Wijnands R., van der Klis M., 1999, *ApJ*, 514, 939
- Wilms J., Allen A., McCray R., 2000, *ApJ*, 542, 914
- Yoon S.-C., Langer N., Scheithauer S., 2004, *A&A*, 425, 217
- Yu W., van der Klis M., 2002, *ApJ*, 567, L67

- Zdziarski A. A., Johnson W. N., Magdziarz P., 1996, MNRAS, 283, 193
- Zhang G., Méndez M., Altamirano D., 2011, MNRAS, 413, 1913
- Zhang W., Lapidus I., Swank J. H., White N. E., Titarchuk L., 1997, IAU Circ., 6541, 1
- Życki P. T., Done C., Smith D. A., 1999, MNRAS, 309, 561